INTERNATIONAL JOURNAL OF HYDROGEN ENERGY 47 (2022) 7168–7179

Available online at www.sciencedirect.com

ScienceDirect

journal homepage: www.elsevier.com/locate/he

Okra-like hollow $Cu_{0.15}$-CoP/Co_3O_4@CC nanotube arrays catalyst for overall water splitting

Xiangheng Du [a], *Jiajun Wang* [b], *Yini Fang* [a], *Yuanjian Liu* [a], *Yudong Wu* [a], *Jibiao Guan* [a], *Shanshan Li* [a], *Lina Wang* [a], *Shulai Lei* [c], *Ming Zhang* [a,*]

[a] *School of Materials Science and Engineering, Zhejiang Sci-Tech University, Hangzhou 310018, PR China*
[b] *Tianjin Key Laboratory of Structure and Performance for Functional Molecules, College of Chemistry, Tianjin Normal University, Tianjin 300387, PR China*
[c] *Hubei Key Laboratory of Low Dimensional Optoelectronic Materials and Devices, Hubei University of Arts and Science, Xiangyang 441053, PR China*

HIGHLIGHTS

- $Cu_{0.15}$-CoP/Co_3O_4@CC has an okra-like hollow nanotube arrays structure.
- The initial overpotential is 13 mV and 225 mV for HER and OER.
- To achieve 10 mA cm^{-2}, a voltage of 1.487 V is required for OWS.
- The $|\Delta G_{H*}|$ of $Cu_{0.15}$-CoP/Co_3O_4@CC is 0.077 eV (Pt: 0.090 eV).

GRAPHICAL ABSTRACT

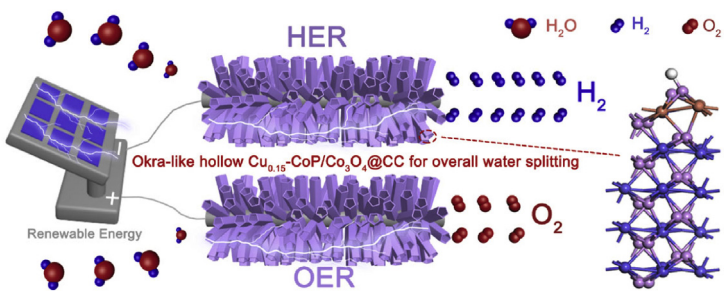

ARTICLE INFO

Article history:
Received 5 July 2021
Received in revised form
22 September 2021
Accepted 6 December 2021
Available online 29 December 2021

Keywords:
Okra-like hollow $Cu_{0.15}$-CoP/Co_3O_4@CC
HER
OER
OWS
Density functional theory

ABSTRACT

The manufacture of hydrogen energy by overall water splitting (OWS) has been broadly considered as a promising candidate for constant energy systems. Herein, we report an okra-like hollow $Cu_{0.15}$-CoP/Co_3O_4@CC nanotube arrays catalyst through a simple hydrothermal-phosphating method. As a noble-metal-free catalyst, it exhibits outstanding HER (hydrogen evolution reaction) catalytic activity with an overpotential of 13 mV to achieve 10 mA cm^{-2} in 1 M KOH electrolyte. For OER (oxygen evolution reaction), it demands 225 mV to achieve 10 mA cm^{-2}. When okra-like hollow $Cu_{0.15}$-CoP/Co_3O_4@CC is used as both cathode and anode electrode materials, 1.487 V is required to reach 10 mA cm^{-2} for OWS, better than numerous electrocatalysts that have been reported. Moreover, it displays excellent stability in a continuously 60 h i-t test, proving an enormous potential for large-scale applications. The theoretical calculation of density functional theory (DFT) further reveals that Cu doping can bring localized structure polarization and reduce the hydrogen adsorption free energy (ΔG_{H*}) on the interstitial sites, thus leading to a significant increase in catalytic activity.

* *Corresponding author.*
E-mail address: zhangming@zstu.edu.cn (M. Zhang).
https://doi.org/10.1016/j.ijhydene.2021.12.055

Introduction

With the development of society, the problem of energy crisis and global warming need to be solved urgently [1]. Hydrogen energy with high weight energy density (142 MJ kg^{-1}) has been used to establish a globally sustainable energy system [2]. Hydrogen production by water splitting is a common approach and can be combined with solar energy and wind energy to reduce electricity consumption [3]. But as a strongly uphill reaction, water splitting in the actual production process often requires higher voltage and energy consumption [4].

Currently, the most excellent HER and OER catalysts are still Pt-based precious metal catalysts and Ir/Ru-based precious metals. Unfortunately, the high price and low storage make it difficult to further promote and large-scale applications [5]. Non-noble-metal OWS catalysts as both anode and cathode electrodes in a single electrochemical device to catalyze HER and OER simultaneously have been regarded as a candidate to reduce energy losses [6]. Alkaline OWS as a low-cost mature technology has been applied to industrial and commercial hydrogen production [7]. In recent decades, researchers put massive effort into transition-metal compounds [8], such as: phosphides [9,10], oxides [11], hydroxide [12,13], layer double hydroxides (LDHs) [14,15], etc. Among them, cobalt phosphide stands out for its unique electronic structure with abundant uncoordinated electrons, but there still is room for improvement. One of the most pragmatic strategies is heteroatom doping, which can tune the crystal structures and enhance the catalytic properties [16]. For instance, Guan and co-works [17] reported a Mo-doped CoP catalytic material for water splitting, which combines electronic structure modification with high-density reaction sites through a doping method. Wen et al. [18] reported a V–Ni_2P NSAs/CC catalyst, which exhibits outstanding HER catalytic performance.

In this work, we prepared Cu_x-CoP/Co_3O_4@CC catalysts with different Cu-doping for water splitting. The substrate carbon cloth can improve the electron transfer efficiency between nanotube arrays and the base. SEM and HAADF-STEM results show that $Cu_{0.15}$-CoP/Co_3O_4@CC catalyst has an okra-like hollow nanotube arrays structure and there are many defects on the surface of the catalyst. The results of the electrochemical analysis indicated that for the cathode HER catalytic reaction, driving 10 mA cm^{-2} only needs 13 mV. Anodic OER requires an overpotential of 225 mV. When okra-like hollow $Cu_{0.15}$-CoP/Co_3O_4@CC is applied as both cathode and anode materials, 10 mA cm^{-2} can be attained with 1.487 V, which has great potential to substitute fossil fuels with serious pollution and limited storage. For potential mechanism explanation, DFT calculation is adopted, proving that Cu doping leads to the electric field polarization of local electrons, thus accelerating the hydrogen adsorption and desorption process of catalysts, thereby enhancing catalytic activity.

Experimental section

Chemical reagents and materials

Carbon cloth (CC, WOS1009) was obtained from CeTech Co., Ltd. Cobalt nitrate hexahydrate ($Co(NO_3)_2 \cdot 6H_2O$) was provided by Shanghai Maclin Biochemical Co., Ltd. Urea (CH_4N_2O), ammonium fluoride (NH_4F), acetate monohydrate ($C_4H_6CuO_4 \cdot H_2O$), and sodium hypophosphite (NaH_2PO_2) were purchased from Shanghai Aladdin.

Synthesis of $Cu_{0.15}$-CoP/Co_3O_4@CC catalysts

Fig. 1 illustrates the synthesis process of the okra-like hollow $Cu_{0.15}$-CoP/Co_3O_4@CC nanotube arrays catalyst. Typically, $Cu_{0.15}$-CoP/Co_3O_4@CC was synthesized by the hydrothermal-phosphating method, which was simple, reliable, and high repeatability. Using carbon cloth as a substrate can provide a large and stable three-dimensional framework to support catalysts with smaller resistance for charge transport. In detail, the preparation process of a series of Cu_x-CoP/Co_3O_4@CC catalysts are as follows. Firstly, 2 mM $Co(NO_3)_2 \cdot 6H_2O$, (0 mM, 0.1 mM, 0.2 mM, 0.3 mM, 0.4 mM, and 0.5 mM) $C_4H_6CuO_4 \cdot H_2O$, corresponds to different Cu doping levels: 0%, 5%, 10%, 15%, 20%, and 25%, 6 mM NH_4F, and 10 mM CH_4N_2O were added in 30 mL H_2O. After magnetic stirring at 500 rpm for 20 min, the mixed solution and carbon cloth (1 cm × 4 cm, clean with HNO_3, C_2H_5OH, and H_2O) are put into a hydrothermal reactor with polytetrafluoroethylene lining. The oxide hydroxide precursor grown on the carbon cloth was obtained after hydrothermally heated at 120 °C for 6 h. In the phosphating process, 0.5 g NaH_2PO_2 was put in the upstream of a porcelain boat. During phosphating, increase from room temperature to 400 °C at a rate of 5 °C min^{-1}, and keep at 400 °C for 2 h in an argon atmosphere (Ar, 150 sccm). Finally, CoP/Co_3O_4@CC, $Cu_{0.05}$-CoP/Co_3O_4@CC, $Cu_{0.1}$-CoP/Co_3O_4@CC, $Cu_{0.15}$-CoP/Co_3O_4@CC, $Cu_{0.2}$-CoP/Co_3O_4@CC, and $Cu_{0.25}$-CoP/Co_3O_4@CC were prepared.

Synthesis of Pt/C catalyst

10 mg 20 wt% Pt/C powder was added into 1 mL solution containing 50 μL 0.5 wt% Nafion and 0.95 mL ethanol for 20 min of ultrasonic treatment. The mixed solution is then transferred to the CC surface several times. Finally, a Pt/C electrode was prepared.

Material characterization

The morphology of prepared catalysts was characterized by scanning electron microscopy (SEM, JSM-6700, JEOL, Japan). The crystal structure was analyzed by high-resolution transmission electron microscopy (HRTEM, JSM-2100, JEOL, Japan), and high-angle annular dark-field scanning transmission

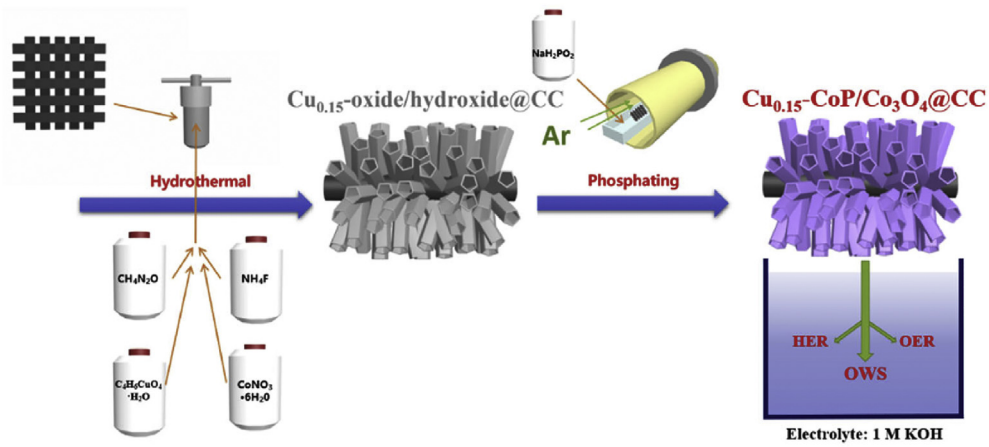

Fig. 1 – Schematic preparation of okra-like hollow $Cu_{0.15}$-CoP/Co_3O_4@CC.

electron microscopy (HAADF-STEM, Tecnai G2 F30S-Twin, Philips-FEI). The angle range of the X-ray diffraction (XRD, D8 DISCOVER, Cu K α radiation (λ = 0.15419 nm), Germany Brook AXS Co., Ltd.) spectra is 10–80°, and the working voltage is 40 kV. Chemical composition and valence state information was conducted on an X-ray photoelectron spectrometer (XPS, Thermo Kalph; Thermo ESCALAB 250XI; Axis Ultra DLD Kratos AXIS SUPRA; PHI-5000versaprobell) with an Al (mono) Kα source (1486.6 eV). The Brunauer Emmett Teller (BET) test is measured by ASAP 2020 (McMuritik (Shanghai) Instrument Co., Ltd.), the test conditions are 77 k nitrogen, degassing 2 h.

Electrochemical measurements

Electrochemical tests were tested by CHI 660 E electrochemical workstation (CH Instruments, Inc., Shanghai). Generally, the prepared catalysts were used as the working electrode with a reference electrode of Hg/HgCl. The saturated calomel electrode (SCE) was calibrated to a reversible hydrogen electrode (RHE) by the calculation: E (E *vs.* RHE) = E (*vs.* SCE) + 0.242 ($E_{Hg/HgCl}$) + 0.592 PH [19]. The overpotential of OER (η^{OER}) was calibrated by the calculation: $\eta^{OER} = \Delta G_{max}/e - 1.23$ V. The sweep rate of the linear sweep voltammetry (LSV) curve is 1 mV s^{-1}. The Tafel slope is obtained by the formula ($\eta = b \log|j| + a$, where η is the overpotential, *j* is the current density, and b is the Tafel slope) [20]. The electrochemical double-layer capacitance (C_{dl}) was determined from the CV curves with a serious scan rate (10–100 mV s^{-1}) by the calculation: $C_{dl} = i/\nu$ (where i is the charging current, and ν is the scan rate). The interfacial charge-transfer resistance was performed by electrochemical Impedance Spectrum (EIS, 10^5-0.01 Hz) within the frequency range of [21].

DFT calculations

All calculations were carried out with density functional theory within the projected-augmented plane wave method [22] as implemented in Vienna ab initio simulation package (VASP) [23]. The generalized gradient approximation as suggested by Perdew, Burke and Ernzerhof with London dispersion corrections as proposed by Grimme (PBE + D2) was employed to accurately describe the weak interaction [24,25]. The Monkhorst-Pack mesh are used to sample the Brillouin zone for geometry optimizations and electronic structure calculations [26]. In our calculations, a plane-wave cutoff energy of 500 eV is used, all atomic positions are relaxed at the PBE level until the atomic forces are less than 0.01 eV/Å, and the tolerance for energy convergence was set to 10^{-5} eV. To minimize the interlayer interactions under the periodic boundary condition, the vacuum spacing is set to be 18.0 Å.

Results and discussion

SEM (Fig. 2a and b) tests confirm that $Cu_{0.15}$-CoP/Co_3O_4@CC processes an okra-like polygonal hollow nanotube structure. X-ray diffraction patterns (XRD, Fig. 2c) of prepared CoP/Co_3O_4@CC, $Cu_{0.05}$-CoP/Co_3O_4@CC, $Cu_{0.1}$-CoP/Co_3O_4@CC, $Cu_{0.15}$-CoP/Co_3O_4@CC, $Cu_{0.2}$-CoP/Co_3O_4@CC, and $Cu_{0.25}$-CoP/Co_3O_4@CC catalysts. The diffraction peaks at 32.6°, 46.2°, 48.4°, and 56.8° are attributed to the (011), (112), (202), and (301) planes of CoP (PDF#29-0497). Besides, a diffraction peak at 36.8° corresponding to the (311) crystal plane of Co_3O_4 (PDF#42-1476), indicating the presence of cobalt oxide in the catalytic material. The two peaks at the diffraction angles of 35.8° and 44.0° are the (211) and (220) of Cu_4O_3 (PDF#49-1830), which confirms the existence of copper oxide. Cu_4O_3 and Co_3O_4 are potential OER catalytic activity centers. The presence of oxides is due to the incomplete phosphating in the preparation process and the oxidation.

From the high-angle annular dark-field scanning transmission electron microscopy (HAADF-STEM) images in Fig. 2d–f, it can be seen that $Cu_{0.15}$-CoP/Co_3O_4@CC has a hollow structure with an outer diameter up of about 215 nm and an inner diameter up of about 129 nm. Lattice defects and distortions can also be seen in Fig. 2e and f, which indicates that the doping of Cu ions leads to the recombination of atoms [27,28]. Furthermore, the existence of defects could provide more active edge sites and faster electron transfer kinetics [29]. The interplanar spacings of 0.286 nm, 0.255 nm, and 0.249 nm match the (103), (112), and (201) crystal planes of CoP (PDF# 29-0497), respectively. Moreover, the interplanar

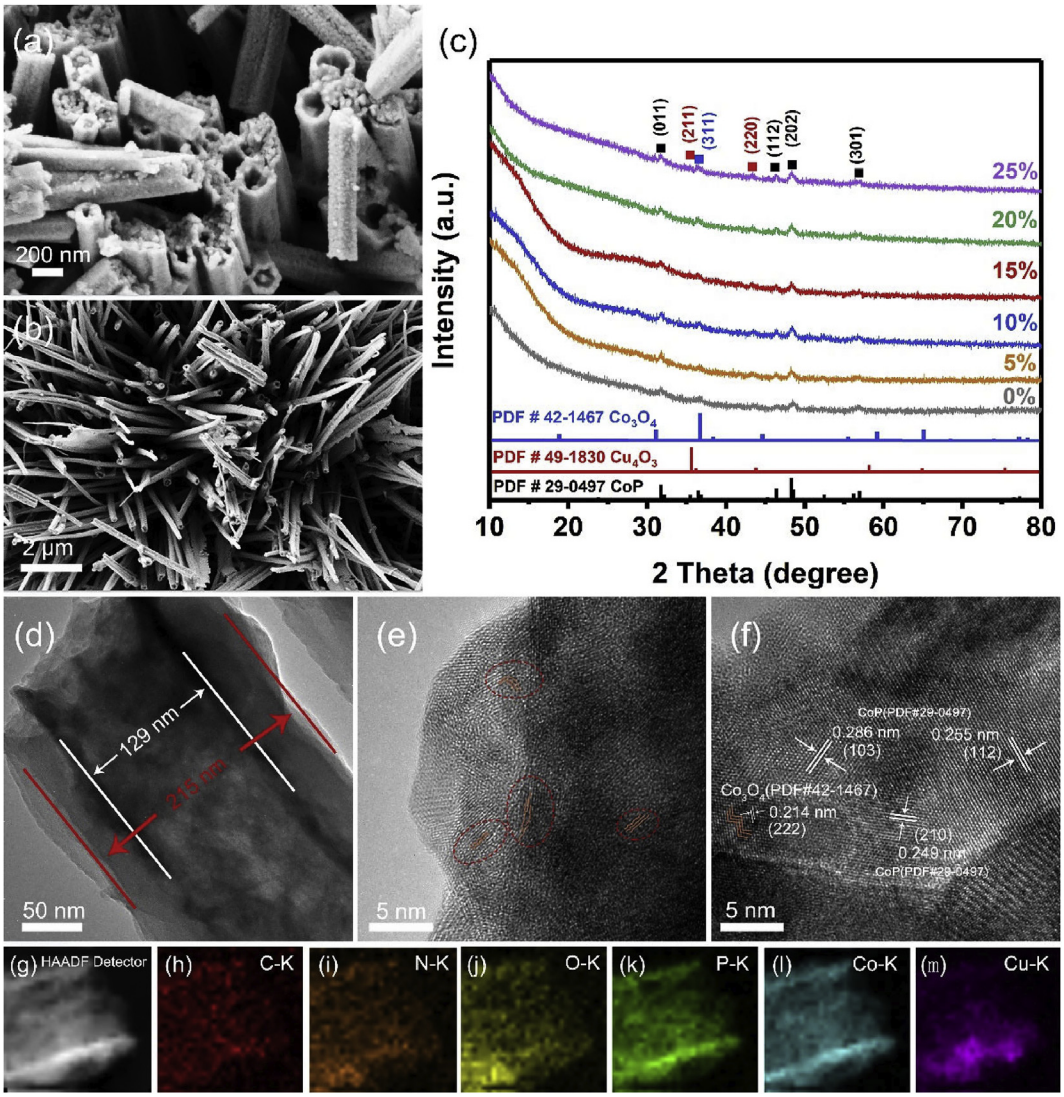

Fig. 2 – (a, b) SEM images of okra-like hollow $Cu_{0.15}$-CoP/Co_3O_4@CC. (c) XRD patterns of Cu_x-CoP/Co_3O_4@CC with different Cu doping percentages. (d) The HAADF-STEM image and (e, f) the crystal structure characterization images of okra-like hollow $Cu_{0.15}$-CoP/Co_3O_4@CC. (g–m) The STEM-EDX elemental mapping of different elements.

spacing of 0.214 nm at the defect region corresponds to the (222) crystal plane of Co_3O_4 (PDF#42-1476), indicating that there is a large amount of oxide at the defect, which corresponds to the potential OER active center. The energy-dispersive X-ray elemental mapping images (EDX) reveals the existence of C, N, O, P, Co, and Cu (Fig. 2g–m) and the uniform doping of Cu atoms. Besides, in Fig. S4, the result of STEM-EDS (Energy Dispersive Spectrometer) further proved the successful doping of Cu atoms.

SEM images (Fig. S1) compares the morphology of $Cu_{0.15}$-CoP/Co_3O_4@CC before and after Cu doping. Fig. S2 explores the morphology of Cu_x-CoP/Co_3O_4@CC with different Cu doping levels. To further explore the influence of doping amount on the structure, we carried out HRTEM characterization on these catalysts with different Cu doping contents from 5% to 25%. From HRTEM (Fig. S3) images we can measure the outer diameters of $Cu_{0.05}$-CoP/Co_3O_4@CC, $Cu_{0.1}$-CoP/Co_3O_4@CC, $Cu_{0.15}$-CoP/Co_3O_4@CC, $Cu_{0.2}$-CoP/Co_3O_4@CC, and $Cu_{0.25}$-CoP/Co_3O_4@CC are 105.4, 159.8, 197.3, 145.3, and 111.6 nm, respectively. And the inner diameters are 64.2, 73.9, 113.8, 60.7, and 0 nm, in that order respectively. Based on the above results, as the Cu doping amount increases from 5% to 15%, both the inner and outer diameters gradually increase. However, excessive Cu doping (from 15% to 25%) can cause the hollow structure to decrease and disappear. The hollow nanotube structure not only exposes larger specific surface areas but also provides reaction channels for reactant diffusion into the inner layer. The acknowledged positive impact, the larger the specific surface areas, the higher the electrochemical active center and catalytic activity, to electrochemical properties, make $Cu_{0.15}$-CoP/Co_3O_4@CC the best catalyst for electrocatalysis water in this system [30,31].

BET test was employed to analyze the porous structure. The N_2 adsorption-desorption isotherm measured of $Cu_{0.05}$-CoP/Co_3O_4@CC, $Cu_{0.1}$-CoP/Co_3O_4@CC, $Cu_{0.15}$-CoP/Co_3O_4@CC, $Cu_{0.2}$-CoP/Co_3O_4@CC, and $Cu_{0.25}$-CoP/Co_3O_4@CC with different

Cu doping amounts at 77 K is shown in Fig. S5a. The isotherm is classified as a typical II isotherm with a hysteresis loop [32]. The adsorption and desorption isotherms show the largest adsorption amount for $Cu_{0.15}$-CoP/Co_3O_4@CC, indicating a bigger specific surface area of 31.3 m^2 g^{-1} and a pore volume of 0.162 mL g^{-1}. Moreover, Fig. S5b indicates the BJH method (desorption) differential integral pore area logarithmic distribution curves of catalysts with different Cu doping amounts and their mesopore peaks. Okra-like hollow $Cu_{0.15}$-CoP/Co_3O_4@CC nanotube structure presents a higher and wider spectrum, reflecting its larger average hole diameter and pore area, which supports the above HRTEM claims.

The X-ray photoelectron spectra (XPS) survey spectra for $Cu_{0.05}$-CoP/Co_3O_4@CC, $Cu_{0.1}$-CoP/Co_3O_4@CC, $Cu_{0.15}$-CoP/Co_3O_4@CC, $Cu_{0.2}$-CoP/Co_3O_4@CC, and $Cu_{0.25}$-CoP/Co_3O_4@CC with different Cu doping are shown in Fig. 3a. The peak of Cu 2p becomes stronger with the increase of doping amount. Fig. 3b is a comparison of the XPS survey peaks before and after 15% Cu doping. The difference is that Cu 2p peaks appear in the XPS survey after Cu doping, indicating the successful doping of Cu. The two peaks at 932.2 eV and 952.1 eV in the XPS spectrum of the Cu 2p region in Fig. 3c are Cu^{2+} [33]. The two satellite peaks are located at 943.5 eV and 943.8 eV. Moreover, only when the doping amount is 10–20%, the low-valent state Cu^{+} peak is present. Further analysis shows that when the doping amount is 15%, the Cu^{+} peaks of $Cu_{0.15}$-CoP/Co_3O_4@CC at 934.9 eV and 954.8 eV are stronger, indicating that it has more Cu^{+} and lower Cu^{2+}/Cu^{+}. Compared with Cu^{2+}, low-valent Cu^{+} and Cu^{2+}/Cu^{+} are more conducive in oxidation reactions, leading to the generation of oxides, which can enhance the OER catalytic activity [34]. In Figs. 3d, 778.4 and 793.3 eV are assigned to Co^{3+}, and Co^{2+} correspond to 781.4 and 798.3 eV [35]. Besides, the peak at 802.2 eV is a satellite peak. The P 2p region spectrum at 129.3 eV and 130.2 eV (Fig. 3e) can be assigned to Cu–P and Co–P bonds [18]. Peaks at 133.8 eV and 134.1 eV are P–O bonds. When the doping amount of Cu is 15%, it shows lower binding energy of 133.8 eV, which is attributed to the increase of oxides and the transfer of electrons from P to O [36,37]. Fig. 3f, the O 1s region of 531.3 eV accordance to Cu–O and Co–O bonds. Furthermore, the peak at 532.9 eV corresponds to the O–H [38].

Except for XPS tests with different doping levels, we also analyzed the changes in XPS before and after Cu doping. As presented in Fig. 3g, the Co 2p region of $Cu_{0.15}$-CoP/Co_3O_4@CC and CoP/Co_3O_4@CC. 778.4 eV and 793.3 eV are attributed to the peaks of Co^{3+}, 781.4 eV and 798.3 eV correspond to the peaks

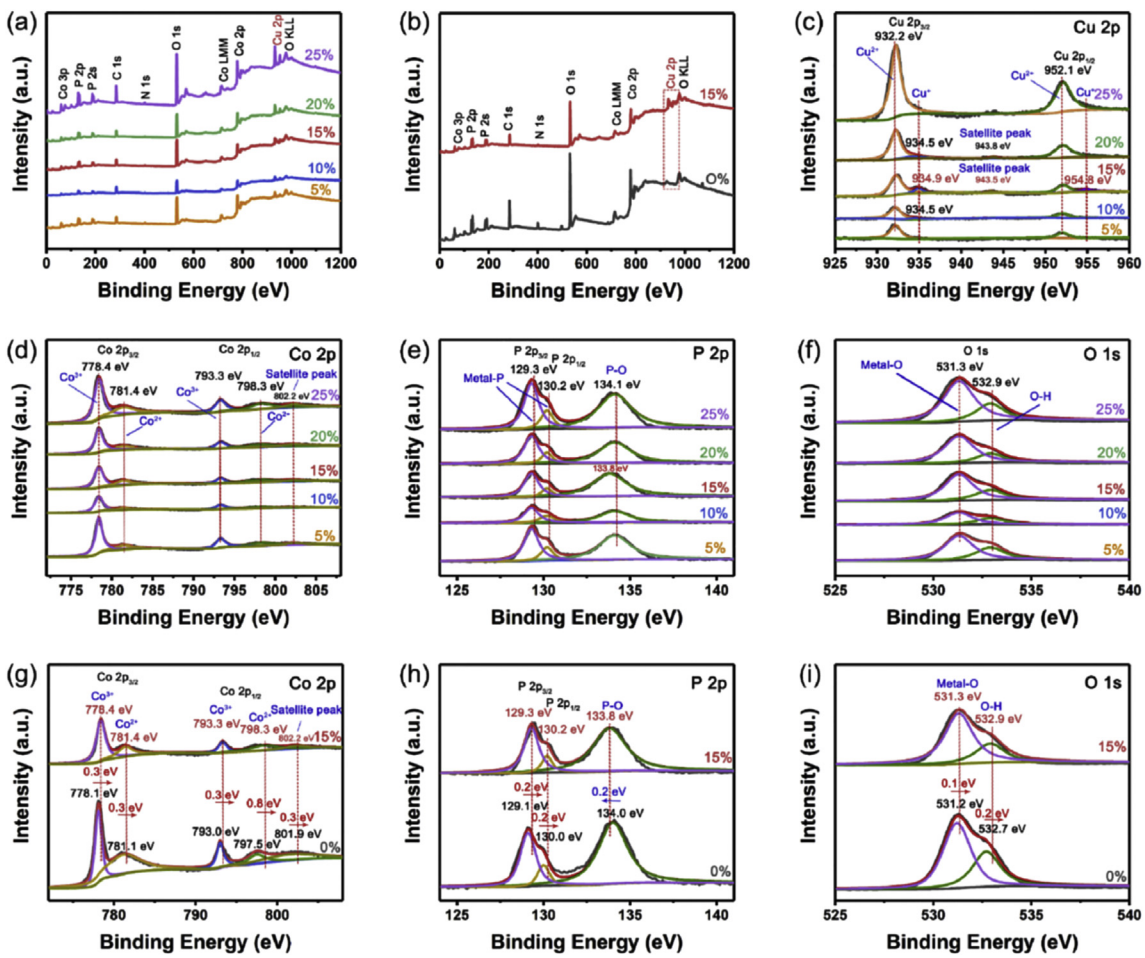

Fig. 3 – The XPS tests of (a) Cu_x-CoP/Co_3O_4@CC catalysts with different Cu doping, (b) $Cu_{0.15}$-CoP/Co_3O_4@CC and CoP/Co_3O_4@CC. (c–f) The XPS tests of (c) Cu 2p, (d) Co 2p, (e) P 2p, and (f) O 1s in Cu_x-CoP/Co_3O_4@CC catalysts with different Cu doping. (g–i) The XPS tests of (g) Co 2p, and (h) P 2p, and (i) O 1s in $Cu_{0.15}$-CoP/Co_3O_4@CC and CoP/Co_3O_4@CC.

of Co^{2+} [35]. In addition, the shift of the spectral peak and the weakening of the peak intensity are attributed to the formation of Cu–P bonds, indicating that Cu successfully doped the Co–P bonds in the catalytic material [39]. The P 2p region (Fig. 3h) of $Cu_{0.15}$-CoP/Co_3O_4@CC at 129.3 eV and 130.2 eV are assigned to Cu–P and Co–P bonds. The shift of the binding energy to higher reveals the formation of Cu. The peak at 133.8 eV is P–O bond [37]. The shift of the binding energy to lower is attributed to the increase of oxides and the transfer of electrons from P to O [40]. Fig. 3i shows the XPS comparison of the O 1 S region before and after doping. The peak at 531.3 eV is attributed to O–Cu and O–Co, and 532.9 eV matches O–H [41]. The XPS peak of O1s shifts to the direction of high binding energy due to the formation of Cu_4O_3 requires more electrons and the transfer of electrons from O to Cu [42].

All the above XPS results show that the atomic valences and binding energies shift. The comparative analysis of XPS with different doping levels indicated that the formation of Cu–P bonds and the increase of Cu^+ in $Cu_{0.15}$-CoP/Co_3O_4@CC. Low price of Cu^+ is conducive to the oxidation reaction, which is advantageous to improve the electron transfer of OER. The comparative analysis before and after XPS doping shows that the shift of binding energy and the weakening of peak intensity are mainly due to the successful doping of Cu and the increase in defects. In addition, we can infer the transfer of electrons from P to O and from O to Cu, proving that the electronic environment on the catalyst surface has been adjusted.

The electrochemical workstation was used to study the catalytic performance of as-prepared catalysts. We firstly evaluated the catalytic HER activity of Cu_x-CoP/Co_3O_4@CC. In Fig. 4a, the HER catalytic activity of Cu_x-CoP/Co_3O_4@CC increases with the dopant concentration up to 15%. Unfortunately, the catalytic activity will decrease with excessive dopants. It can be seen the SEM and HRTEM images of Cu_x-CoP/Co_3O_4@CC from Figs. S2 and S3, compared with $Cu_{0.05}$-CoP/Co_3O_4@CC, $Cu_{0.1}$-CoP/Co_3O_4@CC, $Cu_{0.2}$-CoP/Co_3O_4@CC, and $Cu_{0.25}$-CoP/Co_3O_4@CC, the $Cu_{0.15}$-CoP/Co_3O_4@CC catalyst with 15% Cu doping amount processes a hollow nanotube structure with bigger diameter. The larger inner and outer diameter corresponds to a larger specific surface area and catalytic activity.

Tafel slope can be derived from the LSV polarization curve to deduce the potential HER mechanism. In Fig. 4b, the Tafel slopes of $Cu_{0.05}$-CoP/Co_3O_4@CC, $Cu_{0.1}$-CoP/Co_3O_4@CC, $Cu_{0.15}$-CoP/Co_3O_4@CC, $Cu_{0.2}$-CoP/Co_3O_4@CC, and $Cu_{0.25}$-CoP/Co_3O_4@CC are 155.9, 124.8, 95.8, 135.7, and 191.4 mV dec^{-1}, respectively [43]. Under standard conditions, the smaller the Tafel slope value for catalysts, the larger increment of current density with increasing potential. Therefore, $Cu_{0.15}$-CoP/Co_3O_4@CC has the highest electron transfer efficiency and the potential reaction mechanism is summarized as follows. HER is two electro-transfer reactions, and on the cathode surface, two different mechanisms and three possible reactions maybe occur. In the alkaline electrolyte, the reactions are the Volmer reaction, Heyrovsky reaction, and Tafel reaction [44]. Volmer reaction ($H_2O + e^- \rightarrow H^* + OH^-$): a proton from H_2O combines with an electron to form the absorbed hydrogen intermediate (H*). Heyrovsky reaction ($H_2O + e^- + H^* \rightarrow H_2 + OH^-$): the H* combine H_2O molecules and electrons simultaneously to generate an H_2 molecule. Tafel reaction ($2\ H^* \rightarrow H_2$): two H* are joined together chemically to generate an H_2 molecule [45].

The intersection of the EIS curve and the real axis is the ohmic impedance (Rp) in the solution, and the type of electron transmission resistance of the prepared material is the ohmic impedance [46]. In Fig. 4c, the EIS values of $Cu_{0.05}$-CoP/Co_3O_4@CC, $Cu_{0.1}$-CoP/Co_3O_4@CC, $Cu_{0.15}$-CoP/Co_3O_4@CC, $Cu_{0.2}$-CoP/Co_3O_4@CC and $Cu_{0.25}$-CoP/Co_3O_4@CC are 20.47Ω, 16.34Ω, 13.72Ω, 15.04Ω, and 21.80Ω, respectively. Okra-like hollow $Cu_{0.15}$-CoP/Co_3O_4@CC catalyst with a smaller semicircle value indicates the lower charge carrier migration resistance and the better conductivity. Fig. 4d–f compare the potentials required at different current densities. Notably, okra-like hollow $Cu_{0.15}$-CoP/Co_3O_4@CC exhibits the potential of 13 mV, 81 mV, and 130 mV to achieve different current density, which is lower than other catalysts.

The double-layer capacitance (C_{dl}) values were determined by a simple CV test at different scan rates (Fig. S6). In Fig. 4g, the C_{dl} of Cu_x-CoP/Co_3O_4@CC with different Cu doping concentrations are calculated to be 88.4, 154.3, 192.8, 111.2, and 50.5 mF cm^{-2}, respectively. Moreover, the formula of $ECSA = C_{dl}/C_s$ (Cs is a fixed value) indicates that ECSA has a proportional relationship with C_{dl}. Therefore, when the Cu doping amount is 15%, $Cu_{0.15}$-CoP/Co_3O_4@CC has the largest C_{dl} value and ECSA, corresponding to relatively higher catalytic performance. The results of C_{dl} are also consistent with those of HRTEM in Fig. S3, when the doping amount is 15%, the prepared catalyst has the largest inner and outer diameters.

In addition to its catalytic activity, okra-like hollow $Cu_{0.15}$-CoP/Co_3O_4@CC also has strong stability. We conducted continuous CV sweeps and 60 h i-t test. The LSV curves in Fig. 4h exhibit negligible decay before and after 2000 and 5000 cycles, indicating its strong stability. Besides, 60 h i-t test of okra-like hollow $Cu_{0.15}$-CoP/Co_3O_4@CC has negligible volatility, which demonstrates long-term stability.

Except for the excellent HER performance, outstanding OER properties were also found in okra-like hollow $Cu_{0.15}$-CoP/Co_3O_4@CC nanotube arrays catalyst. Fig. 5a demonstrates the representative polarization curves of Cu_x-CoP/Co_3O_4@CC catalysts with different Cu doping amounts. Distinctly, okra-like hollow $Cu_{0.15}$-CoP/Co_3O_4@CC still processes the most excellent catalytic performance. In Fig. 5b, the calculation result of the Tafel slope corresponding to the polarization curve is used to judge the electron conversion efficiency of OER reaction. Fig. 5c and d shows the potentials required at different current densities. The overpotential of okra-like hollow $Cu_{0.15}$-CoP/Co_3O_4@CC nanotube arrays catalyst is 225 mV, which is 150, 104, 123, and 148 mV less than the $Cu_{0.05}$-CoP/Co_3O_4@CC, $Cu_{0.1}$-CoP/Co_3O_4@CC, $Cu_{0.2}$-CoP/Co_3O_4@CC, and $Cu_{0.25}$-CoP/Co_3O_4@CC catalysts, respectively. Moreover, $Cu_{0.15}$-CoP/Co_3O_4@CC with 15% Cu doping requires a potential of only 456 mV to deliver 100 mA cm^{-2}, which is 104, 55, 83, and 124 mV less than the $Cu_{0.05}$-CoP/Co_3O_4@CC, $Cu_{0.1}$-CoP/Co_3O_4@CC, $Cu_{0.2}$-CoP/Co_3O_4@CC, and $Cu_{0.25}$-CoP/Co_3O_4@CC catalysts, respectively. From the above analysis, it can be summarized that for OER, the best Cu doping ratio is still 15%.

We verify the durability of okra-like hollow $Cu_{0.15}$-CoP/Co_3O_4@CC nanotube arrays catalyst through CV accelerated cycle test and i-t test. In Fig. 5e, after 2000 and 5000 cycling

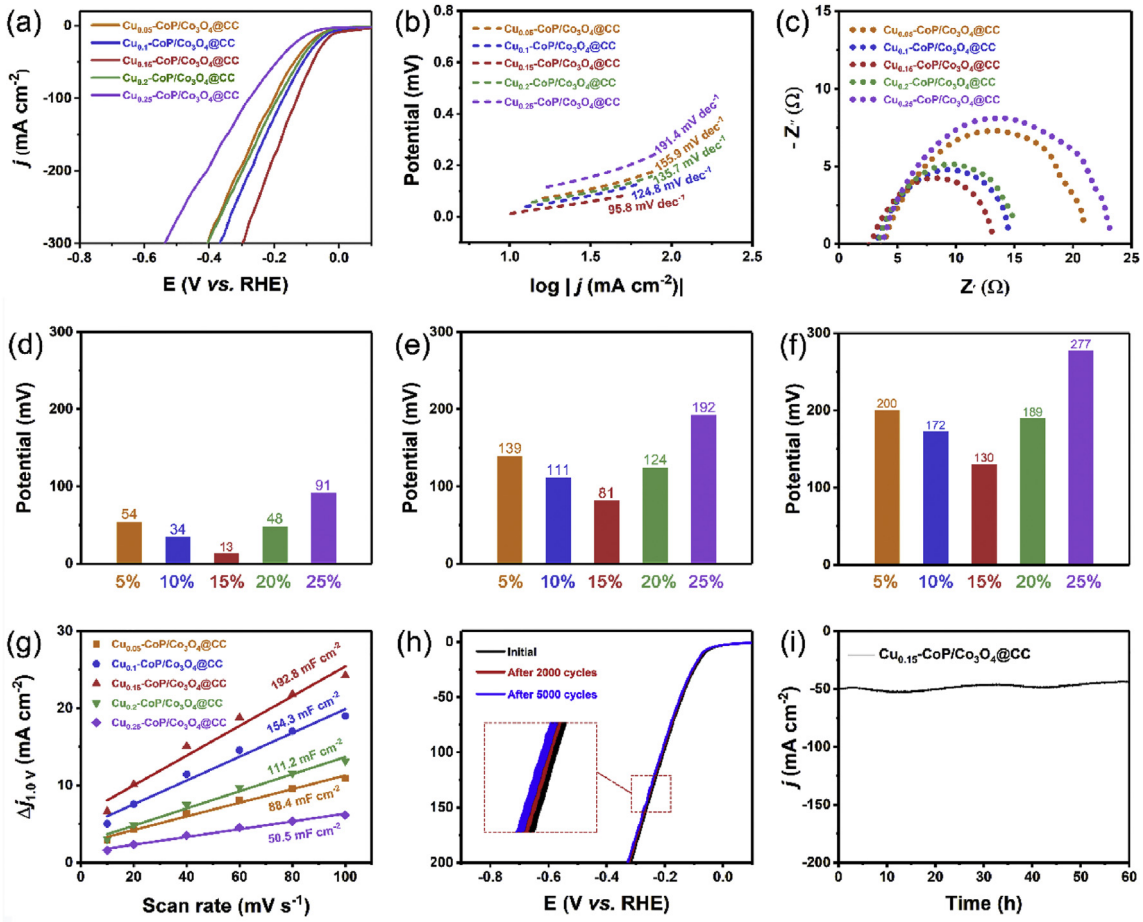

Fig. 4 – Electrocatalytic HER in 1 M KOH. (a) LSV curves, (b) Tafel plots. (c) EIS of Cu_x-CoP/Co_3O_4@CC. (d–f) Comparison of the potentials required at (d) 10, (e) 50, (f) 100 mA cm^{-2}. (g) C_{dl} values of Cu_x-CoP/Co_3O_4@CC. (h) LSV curves before and after CV cycles. (i) 60 h i-t curve.

tests, the change of OER-LSV curves is slight, indicating its excellent durability. Furthermore, in Figs. 5f and 60 h i-t test shows a negligible drop, indicating its durability for OER in alkaline electrolyte.

We further applied okra-like hollow $Cu_{0.15}$-CoP/Co_3O_4@CC nanotube arrays catalyst as both HER and OER catalysts for overall water splitting. Fig. 6a displays the OWS polarization curves of as-prepared Cu_x-CoP/Co_3O_4@CC catalysts with different Cu doping amounts. The corresponding Tafel slope exhibits in Fig. 6b. The okra-like hollow $Cu_{0.15}$-CoP/Co_3O_4@CC has the highest OWS catalytic activity and the lowest Tafel slope. Remarkably, in Fig. 6c, okra-like hollow $Cu_{0.15}$-CoP/Co_3O_4@CC nanotube arrays catalyst only need a low 1.487 V cell voltage to drive 10 mA cm^{-2}, which is 0.12, 0.069, 0.132, and 0.144 V less than that of $Cu_{0.05}$-CoP/Co_3O_4@CC, $Cu_{0.1}$-CoP/Co_3O_4@CC, $Cu_{0.2}$-CoP/Co_3O_4@CC, and $Cu_{0.25}$-CoP/Co_3O_4@CC catalysts, respectively. Additionally, okra-like hollow $Cu_{0.15}$-CoP/Co_3O_4@CC requires a 1.706 V cell voltage to achieve 100 mA cm^{-2}, which surpasses other catalysts. These results manifest the best OWS catalyst in this study is $Cu_{0.15}$-CoP/Co_3O_4@CC with 15% doping amount. Significantly, to apply it in practical applications, a long-term stability test is a must. Consistent with HER and OER, the catalytic activity remains unchanged before and after 2000 and 5000 cycles (Fig. 6e), and a negligible degradation in 60 h i-t test (Fig. 6f), which proves the outstanding stability and promising commercial application potential of okra-like hollow $Cu_{0.15}$-CoP/Co_3O_4@CC catalyst.

To explore the actual production of hydrogen and oxygen, we adopted relatively simple drainage and gas collection method. The specific test results are exhibited in Fig. S7. Under the overpotential of drive 10 mA cm^{-2}, the hydrogen production rate is about 4 mL min^{-1} cm^{-2}, and the oxygen production rate is about 2 mL min^{-1} cm^{-2}. Moreover, the actual production of hydrogen is approximately twice that of oxygen.

For the characterization of the crystal structure after $Cu_{0.15}$-CoP/Co_3O_4@CC after HER and OER tests (20 HER-LSV and OER-LSV tests). From the SEM test results in Fig. S8, we can see that the surface of the hollow nanotubes is covered with some nanocrystals. The XRD test results are demonstrated in Fig. S9. To further explore the crystal structure and the nanocrystals on the surface, we performed HRTEM and XPS tests. It can be seen from Fig. S10 HRTEM images that the hollow nanotube structure is still maintained after the HER test. Moreover, after OER tests, many amorphous regions and oxides are formed on the surface of catalysts. The XPS test results of $Cu_{0.15}$-CoP/Co_3O_4@CC before and after HRHER and OER tests are shown in Fig. S11. We can see that the XPS

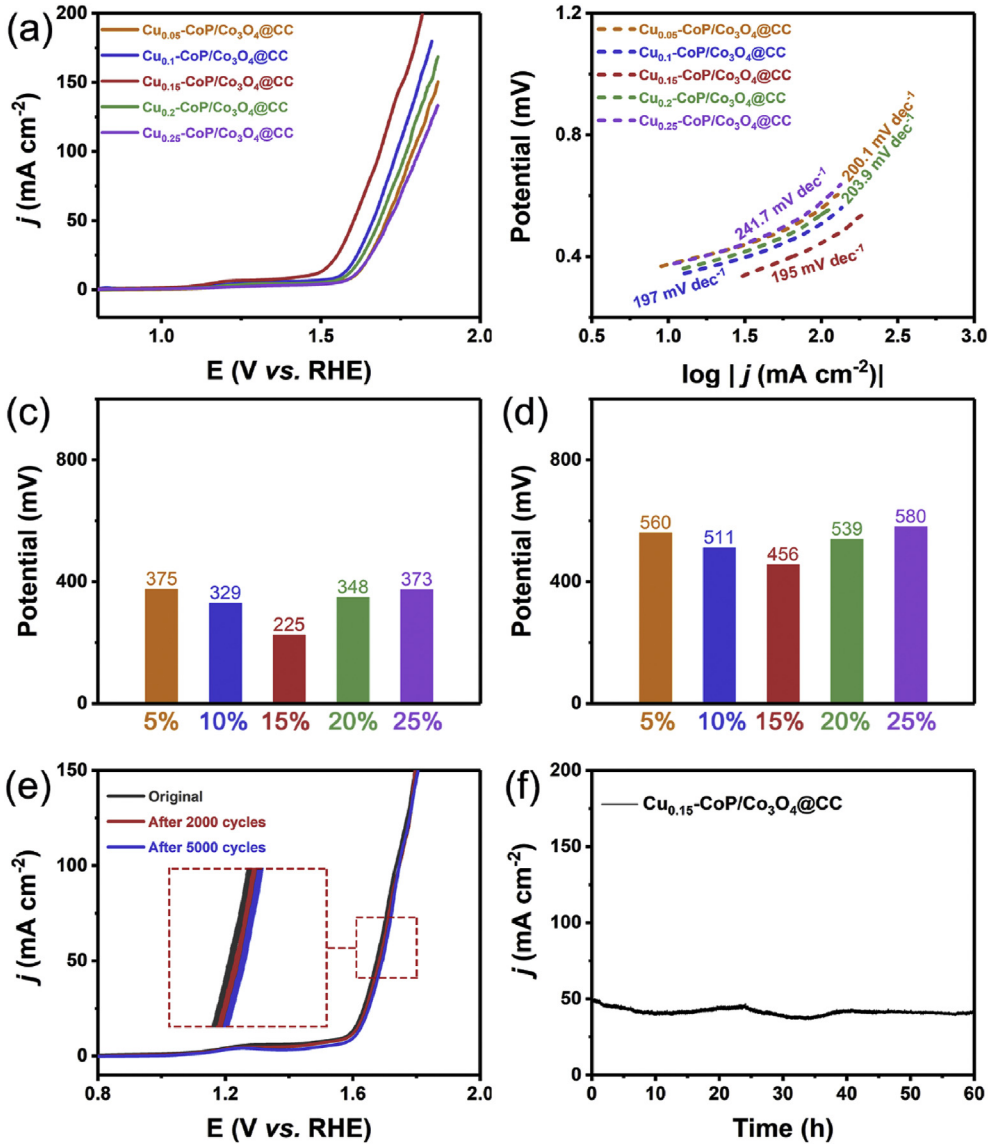

Fig. 5 – Electrocatalytic OER in 1 M KOH. (a) LSV curves of Cu_x-CoP/Co_3O_4@CC. (b) Tafel plots. (c–d) Comparison of the potentials required at (c) 10, (d) 100 mA cm^{-2}. (e) LSV curves before and after CV cycles. (f) The 60 h i-t curve of okra-like hollow $Cu_{0.15}$-CoP/Co_3O_4@CC.

results after the HER test is relatively consistent, and the changes are minor. However, after the OER test, the XPS results of $Cu_{0.15}$-CoP/Co_3O_4@CC have undergone major changes, due to the formation of new nanocrystals and generous oxides during the OER tests. Furthermore, compared to the O 1s peak of the original, the peak after the OER tests is stronger, which is related to the increase of surface oxides on the surface of catalytic material.

In addition to the effects of different doping levels on the morphology and performance of prepared catalysts, we also explore the essential effects before and after Cu doping. Obviously, in Fig. 7a–c, the HER, OER, and OWS performance of okra-like hollow $Cu_{0.15}$-CoP/Co_3O_4@CC catalyst after Cu doping has been improved to a certain extent, indicating that Cu doping can enhance the catalytic activity. From the SEM images in Fig. 7d–f, the CoP/Co_3O_4@CC has a nanowire arrays structure. But after doping, it transfers to an okra-like hollow nanotube arrays structure, due to Cu doping has successfully modulated the growth pattern of $Cu_{0.15}$-CoP/Co_3O_4@CC, which may be related to the difference in atomic diffusion rate and the Kirkendall effect [47,48]. Furthermore, the heteroatom doping strategy successfully adjusted the crystal growth and ultimately improved the catalytic activity.

To verify the reaction mechanism proposed above, we used density functional theory (DFT) to further calculate this group of catalysts with different Cu doping amounts (Supplementary material) [49–51]. The DFT theoretical calculations explored the structural change after Cu doping and the potential mechanism for catalytic performance improvement [52]. In Fig. 8a–e, we investigated the atomic model diagram of Cu_x-CoP/Co_3O_4@CC (101) surface and explored the effect of different Cu doping amounts on Co and P atomic sites. Select (101) plane as the crystal plane for simulation calculation can be attributed to it has better catalytic activity and lower surface

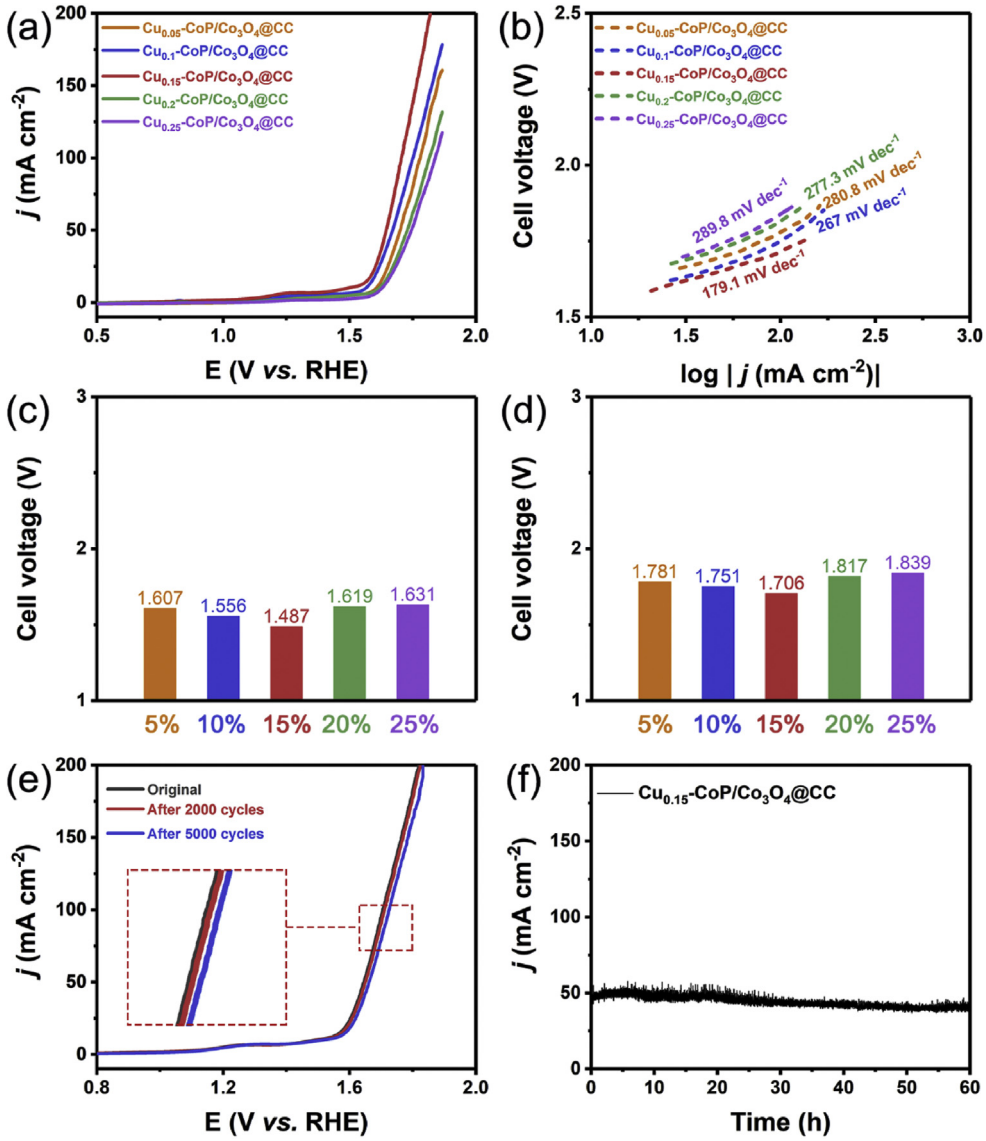

Fig. 6 – Electrocatalytic OWS in 1 M KOH. (a) LSV curves of Cu_x-CoP/Co_3O_4@CC. (b) Tafel plots. (c–d) Comparison of the cell voltages required at (c) 10, (d) 100 mA cm^{-2}. (e) LSV curves before and after CV cycles. (f) 60 h i-t curve.

energy [53,54]. The H* adsorption free energies (ΔG_{H*}) of diverse Cu_x-CoP/Co_3O_4@CC catalysts are presented in Fig. 8f and g. It can be found that the ΔG_{H*} values of okra-like hollow $Cu_{0.15}$-CoP/Co_3O_4@CC (0.077 eV) is closest to the ideal 0 eV, which proves that $Cu_{0.15}$-CoP/Co_3O_4@CC has the faster electron transfer and hydrogen release rate compared with CoP/Co_3O_4@CC (0.159 eV), $Cu_{0.05}$-CoP/Co_3O_4@CC (0.134 eV), $Cu_{0.1}$-CoP/Co_3O_4@CC (0.113 eV), $Cu_{0.2}$-CoP/Co_3O_4@CC (−0.137 eV), $Cu_{0.25}$-CoP/Co_3O_4@CC (−0.243 eV). Surprisingly, compared to the noble metal Pt (−0.09 eV), the ΔG_{H*} of okra-like hollow $Cu_{0.15}$-CoP/Co_3O_4@CC (0.077 eV) is lower, showing the considerable possibility to precious metals.

The generation of hydrogen is mainly divided into two major steps: discharge adsorption process and desorption hydrogen evolution [55]. When $\Delta G_{H*} < 0$, the hydrogen atom is easier to adsorb but unfavorable for desorption. Then, the reaction is controlled by the desorption process. On the contrary, when $\Delta G_{H*} > 0$, the entire reaction is subject to the adsorption process. For a best HER catalyst, it is ideal to reach an equilibrium that the adsorption and desorption rates are equivalent ($\Delta G_{H*} \approx 0$), where the proton/electron-transfer process is balanced so that the two steps can proceed faster simultaneously on the catalyst surface [56]. In our study, the DFT calculations are consistent with experimental results that okra-like hollow $Cu_{0.15}$-CoP/Co_3O_4@CC has a faster hydrogen adsorption and desorption rate.

Based on all the above results and discussions, we summarized the outstanding HER, OER, and OWS performance of okra-like hollow $Cu_{0.15}$-CoP/Co_3O_4@CC nanotube arrays catalyst. (1) Okra-like hollow $Cu_{0.15}$-CoP/Co_3O_4@CC nanotube arrays grown on carbon cloth enables the catalyst to possess closer contact with the substrate, which increases the electrical conductivity and the charge carrier transfer. (2) According to the SEM, TEM, BET, and C_{dl} results, it can be concluded that the okra-like hollow $Cu_{0.15}$-CoP/Co_3O_4@CC nanotube arrays with 15% doping amount has larger outer and

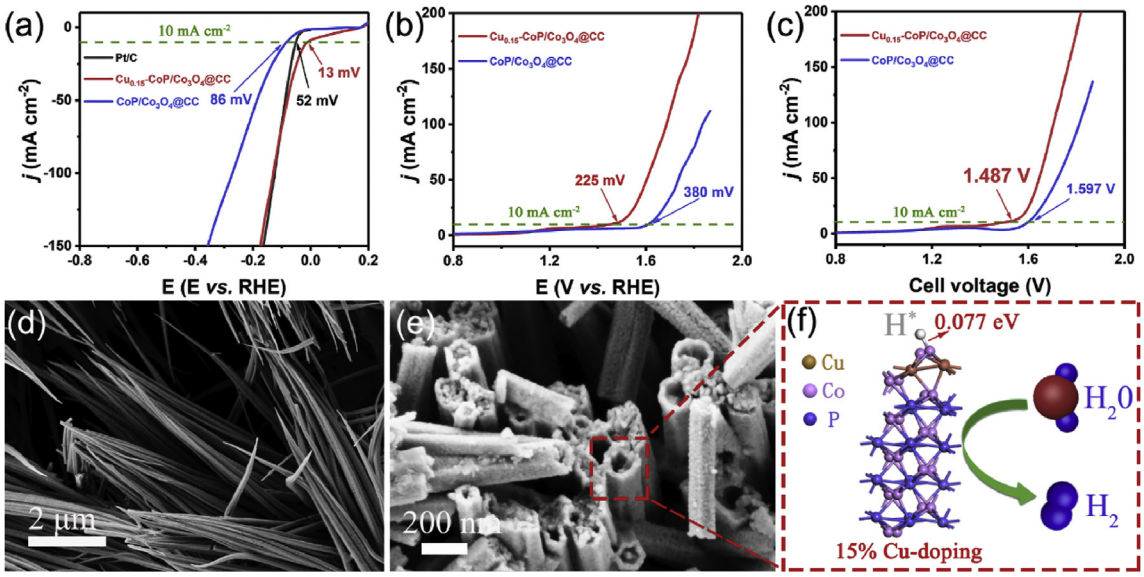

Fig. 7 – Comparisons the polarization curves of HER, OER, and OWS before and after Cu doping. LSV curves of (a) HER, (b) OER, (C) OWS. (d) SEM image of CoP/Co_3O_4@CC. (e) SEM image of okra-like hollow $Cu_{0.15}$-CoP/Co_3O_4@CC. (f) Structural model of okra-like hollow $Cu_{0.15}$-CoP/Co_3O_4@CC.

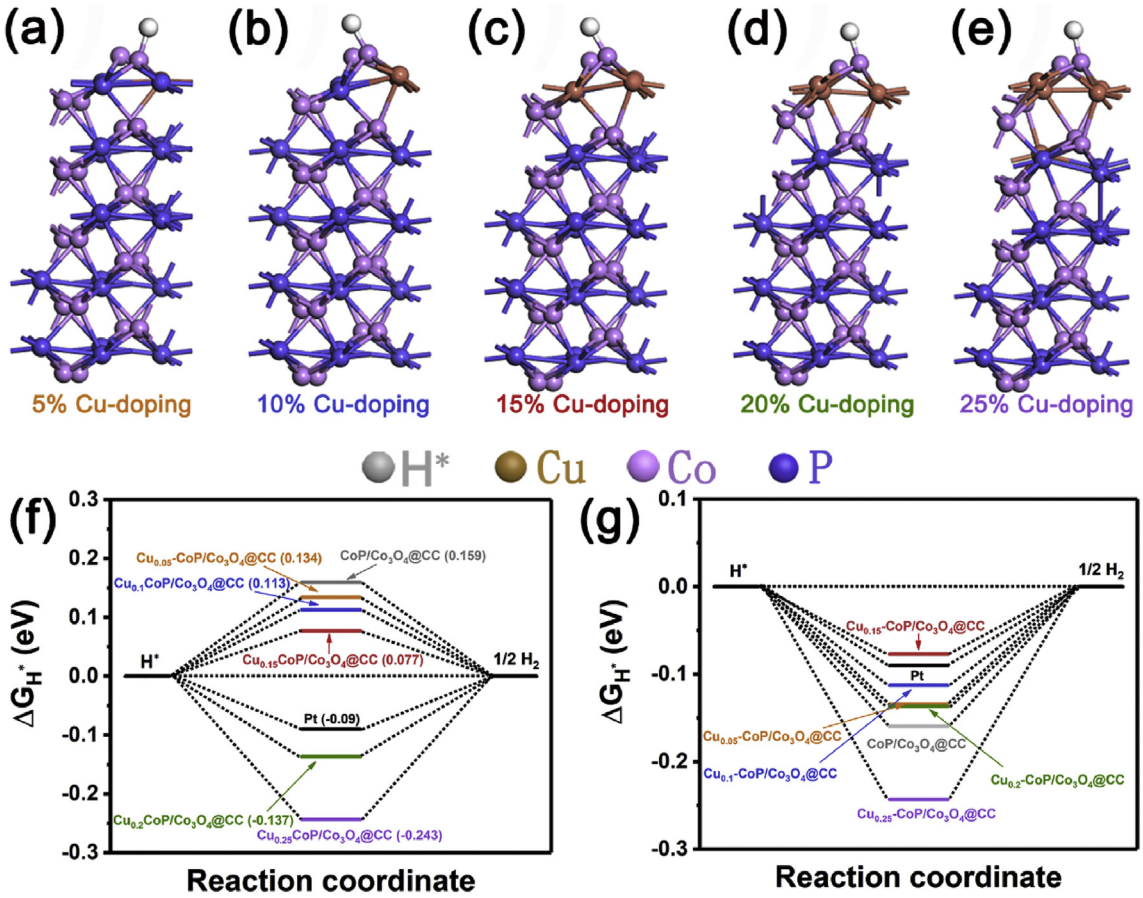

Fig. 8 – (a–e) Atomic structures of different Cu-doping (a) 5%, (b) 10%, (c) 15%, (d) 20%, (e) 25%. (f) The free energy diagram of ΔG_{H^*}. (g) Comparison of the value of $|\Delta G_{H^*}|$ among different catalysts.

inner diameters that can contact with the electrolyte, thereby effectively increasing the electrochemical surface area and HER catalytic performance. (3) According to the HAADF-STEM image, Cu doping leads to lattice defects and distortion, and there are a lot of oxides at the region of the defect, which corresponds to the potential OER active center. (4) XPS results show that the ratio of Cu^{+}/Cu^{2+} is higher in $Cu_{0.15}$-CoP/Co_3O_4@CC. The transfer of electrons from P to O and then to Cu is the internal mechanism for the improvement of OER catalytic activity. In addition, the formation of Cu–P bonds and the reduction of Co–P bonds prove the successful doping of Cu. (5) DFT calculations confirm that okra-like hollow $Cu_{0.15}$-CoP/Co_3O_4@CC has a lower ΔG_{H*} of 0.077 eV (closer to 0 eV), which is the potential mechanism explanation for the increased catalytic activity of electrolyzed water.

Conclusions

In summary, we design and manufacture an okra-like hollow $Cu_{0.15}$-CoP/Co_3O_4@CC nanotube arrays structure catalyst, which is confirmed to be an excellent catalyst for HER, OER, and OWS. The initial overpotentials of HER and OER are 13 and 225 mV in alkaline electrolytes, respectively. Moreover, it requires 1.487 V to drive 10 mA cm^{-2} for OWS. To reach 100 mA cm^{-2}, it demands 1.706 V. For stability, okra-like hollow $Cu_{0.15}$-CoP/Co_3O_4@CC can keep its catalytic activity for 60 h, confirming its high research value. DFT calculations suggest that $Cu_{0.15}$-CoP/Co_3O_4@CC processes a lower ΔGH* of 0.077 eV, which proves the inner mechanism of efficient water splitting.

Declaration of competing interest

The authors declare that they have no known competing financial interests or personal relationships that could have appeared to influence the work reported in this paper.

Acknowledgements

This study was supported by the National Natural Science Foundation of China (Grant No. 51373154, 51573166) and the Science&Technology Development Fund of Tianjin Education Commission for Higher Education (2020KJ008).

Appendix A. Supplementary data

Supplementary data to this article can be found online at https://doi.org/10.1016/j.ijhydene.2021.12.055.

REFERENCES

[1] Xu H, Ci S, Ding Y, Wang G, Wen Z. Recent advances in precious metal-free bifunctional catalysts for electrochemical conversion systems. J Mater Chem A 2019;7:8006–29.
[2] Zhao G, Rui K, Dou SX, Sun W. Heterostructures for electrochemical hydrogen evolution reaction: a review. Adv Funct Mater 2018;28:1803291.
[3] Koutavarapu R, Venkata Reddy C, Babu B, Reddy KR, Cho M, Shim J. Carbon cloth/transition metals-based hybrids with controllable architectures for electrocatalytic hydrogen evolution - a review. Int J Hydrogen Energy 2020;45:7716–40.
[4] You B, Sun Y. Innovative strategies for electrocatalytic water splitting. Accounts Chem Res 2018;51:1571–80.
[5] Yu F, Zhou H, Huang Y, Sun J, Qin F, Bao J, et al. High-performance bifunctional porous non-noble metal phosphide catalyst for overall water splitting. Nat Commun 2018;9:2551.
[6] Arif M, Yasin G, Shakeel M, Mushtaq MA, Ye W, Fang X, et al. Highly active sites of NiVB nanoparticles dispersed onto graphene nanosheets towards efficient and pH-universal overall water splitting. J Energy Chem 2021;58:237–46.
[7] Sun Q, Wang L, Shen Y, Zhou M, Ma Y, Wang Z, et al. Bifunctional copper-doped nickel catalysts enable energy-efficient hydrogen production via hydrazine oxidation and hydrogen evolution reduction. ACS Sustainable Chem Eng 2018;6:12746–54.
[8] Sun H, Yan Z, Liu F, Xu W, Cheng F, Chen J. Self-supported transition-metal-based electrocatalysts for hydrogen and oxygen evolution. Adv Mater 2019;32:1806326.
[9] Yang X, Lu A-Y, Zhu Y, Hedhili MN, Min S, Huang K-W, et al. CoP nanosheet assembly grown on carbon cloth: a highly efficient electrocatalyst for hydrogen generation. Nano Energy 2015;15:634–41.
[10] Xing Z, Liu Q, Asiri AM, Sun X. Closely interconnected network of molybdenum phosphide nanoparticles: a highly efficient electrocatalyst for generating hydrogen from water. Adv Mater 2014;26:5702–7.
[11] Sun J, Li H, Huang Y, Zhuang Z. CoFeW ternary oxides nanoparticles for oxygen evolution reaction. Mater Lett 2018;223:246–9.
[12] Gao R, Yan D. Fast formation of single-unit-cell-thick and defect-rich layered double hydroxide nanosheets with highly enhanced oxygen evolution reaction for water splitting. Nano Res 2018;11:1883–94.
[13] Guo Z, Ye W, Fang X, Wan J, Ye Y, Dong Y, et al. Amorphous cobalt–iron hydroxides as high-efficiency oxygen-evolution catalysts based on a facile electrospinning process. Inorg Chem Front 2019;6:687–93.
[14] Arif M, Yasin G, Luo L, Ye W, Mushtaq MA, Fang X, et al. Hierarchical hollow nanotubes of NiFeV-layered double hydroxides@CoVP heterostructures towards efficient, pH-universal electrocatalytical nitrogen reduction reaction to ammonia. Appl Catal B Environ 2020;265:118559.
[15] Arif M, Yasin G, Shakeel M, Fang X, Gao R, Ji S, et al. Coupling of bifunctional CoMn-layered double Hydroxide@Graphitic C3 N4 nanohybrids towards efficient photoelectrochemical overall water splitting. Chem Asian J 2018;13:1045–52.
[16] Duan J, Chen S, Jaroniec M, Qiao SZ. Heteroatom-doped graphene-based materials for energy-relevant electrocatalytic processes. ACS Catal 2015;5:5207–34.
[17] Guan C, Xiao W, Wu H, Liu X, Zang W, Zhang H, et al. Hollow Mo-doped CoP nanoarrays for efficient overall water splitting. Nano Energy 2018;48:73–80.
[18] Wen L, Yu J, Xing C, Liu D, Lyu X, Cai W, et al. Flexible vanadium-doped Ni2P nanosheet arrays grown on carbon cloth for an efficient hydrogen evolution reaction. Nanoscale 2019;11:4198–203.
[19] Shang X, Chi J-Q, Lu S-S, Dong B, Li X, Liu Y-R, et al. Novel CoxSy/WS2 nanosheets supported on carbon cloth as efficient electrocatalyst for hydrogen evolution reaction. Int J Hydrogen Energy 2017;42:4165–73.
[20] Ma S, Wang L, Zhang S, Jin H, Wan M, Pan Y, et al. Facile fabrication of a binary NiCo phosphide with hierarchical

architecture for efficient hydrogen evolution reactions. Int J Hydrogen Energy 2019;44:4188–96.
[21] Du X, Fang Y, Guan J, Zhang T, Yi L, Wang L, et al. Urchin-like Co0.8-Mn0.2-P/CC nanowires array: a high-performance and cost-effective hydrogen evolution electrocatalyst. Int J Hydrogen Energy 2020;45:18976–84.
[22] Blöchl PE. Projector augmented-wave method. Phys Rev B 1994;50:17953–79.
[23] Lejaeghere K, Bihlmayer G, Bjorkman T, Blaha P, Blugel S, Blum V, et al. Reproducibility in density functional theory calculations of solids. Science 2016;351:aad3000.
[24] Perdew JP, Yang W, Burke K, Yang Z, Gross EKU, Scheffler M, et al. Understanding band gaps of solids in generalized Kohn–Sham theory. Proc Natl Acad Sci Unit States Am 2017;114:2801–6.
[25] Grimme S. Semiempirical GGA-type density functional constructed with a long-range dispersion correction. J Comput Chem 2006;27:1787–99.
[26] Monkhorst HJ, Pack JD. Special points for Brillouin-zone integrations. Phys Rev B 1976;13:5188–92.
[27] Jia Y, Zhang L, Gao G, Chen H, Wang B, Zhou J, et al. A heterostructure coupling of exfoliated Ni-Fe hydroxide nanosheet and defective graphene as a bifunctional electrocatalyst for overall water splitting. Adv Mater 2017;29.
[28] Guo X, Wang L, Zeng J, Shao Y, Cui W, Zhang C, et al. Defect-rich MoS/carbon nanofiber arrays on carbon cloth for highly efficient electrocatalytic hydrogen evolution. Int J Hydrogen Energy 2018;43:23118–25.
[29] Lasia A. Mechanism and kinetics of the hydrogen evolution reaction. Int J Hydrogen Energy 2019;44:19484–518.
[30] Zang X, Chen W, Zou X, Hohman JN, Yang L, Li B, et al. Self-Assembly of large-area 2D polycrystalline transition metal carbides for hydrogen electrocatalysis. Adv Mater 2018;30:1805188.
[31] Do DD, Do HD, Nicholson D. A computer appraisal of BET theory, BET surface area and the calculation of surface excess for gas adsorption on a graphite surface. Chem Eng Sci 2010;65:3331–40.
[32] Jin Y, Wang H, Li J, Yue X, Han Y, Shen PK, et al. Porous MoO2 nanosheets as non-noble bifunctional electrocatalysts for overall water splitting. Adv Mater 2016;28:3785–90.
[33] Du X, Su H, Zhang X. Metal–organic framework-derived Cu-doped Co9S8 nanorod array with less low-valence Co sites as highly efficient bifunctional electrodes for overall water splitting. ACS Sustainable Chem Eng 2019;7:16917–26.
[34] Coşkuner Filiz B, Kantürk Figen A, Pişkin S. The remarkable role of metal promoters on the catalytic activity of Co-Cu based nanoparticles for boosting hydrogen evolution: ammonia borane hydrolysis. Appl Catal B Environ 2018;238:365–80.
[35] Song J, Xiang J, Mu C, Wang B, Wen F, Su C, et al. Facile synthesis and excellent electrochemical performance of CoP nanowire on carbon cloth as bifunctional electrode for hydrogen evolution reaction and supercapacitor. Sci China Mater 2017;60:1179–86.
[36] Pi M, Wu T, Zhang D, Chen S, Wang S. Self-supported three-dimensional mesoporous semimetallic WP2 nanowire arrays on carbon cloth as a flexible cathode for efficient hydrogen evolution. Nanoscale 2016;8:19779–86.
[37] Wang J, Yang W, Liu J. CoP2nanoparticles on reduced graphene oxide sheets as a super-efficient bifunctional electrocatalyst for full water splitting. J Mater Chem A 2016;4:4686–90.
[38] Liu PF, Li X, Yang S, Zu MY, Liu P, Zhang B, et al. Ni2P(O)/Fe2P(O) interface can boost oxygen evolution electrocatalysis. ACS Energy Lett 2017;2:2257–63.
[39] Wen L, Sun Y, Zhang C, Yu J, Li X, Lyu X, et al. Cu-doped CoP nanorod arrays: efficient and durable hydrogen evolution reaction electrocatalysts at all pH values. ACS Appl Energy Mater 2018;1:3835–42.
[40] Du X, Fang Y, Guan J, Li S, Wang L, Zhang M. Vanadium doped cobalt phosphide nanorods array as a bifunctional electrode catalyst for efficient and stable overall water splitting. Int J Hydrogen Energy 2020:599–608.
[41] Svintsitskiy DA, Kardash TY, Stonkus OA, Slavinskaya EM, Stadnichenko AI, Koscheev SV, et al. In situ XRD, XPS, TEM, and TPR study of highly active in CO oxidation CuO nanopowders. J Phys Chem C 2013;117:14588–99.
[42] Sun Y, Li R, Chen X, Wu J, Xie Y, Wang X, et al. A-Site management prompts the dynamic reconstructed active phase of perovskite oxide OER catalysts. Adv Energy Mater 2021;11:2003755.
[43] Li X, Hao X, Abudula A, Guan G. Nanostructured catalysts for electrochemical water splitting: current state and prospects. J Mater Chem 2016;4:11973–2000.
[44] Anantharaj S, Aravindan V. Developments and perspectives in 3d transition-metal-based electrocatalysts for neutral and near-neutral water electrolysis. Adv Energy Mater 2019;10:1902666.
[45] Wang J, Yue X, Yang Y, Sirisomboonchai S, Wang P, Ma X, et al. Earth-abundant transition-metal-based bifunctional catalysts for overall electrochemical water splitting: a review. J Alloys Compd 2020;819:153346.
[46] Cruz-Manzo S, Chen R, Rama P. Study of current distribution and oxygen diffusion in the fuel cell cathode catalyst layer through electrochemical impedance spectroscopy. Int J Hydrogen Energy 2013;38:1702–13.
[47] Ji D, Fan L, Tao L, Sun Y, Li M, Yang G, et al. The Kirkendall effect for engineering oxygen vacancy of hollow Co3 O4 nanoparticles toward high-performance portable zinc-air batteries. Angew Chem 2019;58:13840–4.
[48] Kim M, Seok H, Clament Sagaya Selvam N, Cho J, Choi GH, Nam MG, et al. Kirkendall effect induced bifunctional hybrid electrocatalyst (Co9S8@MoS2/N-doped hollow carbon) for high performance overall water splitting. J Power Sources 2021;493:229688.
[49] He Q, Tian D, Jiang H, Cao D, Wei S, Liu D, et al. Achieving efficient alkaline hydrogen evolution reaction over a Ni5 P4 catalyst incorporating single-atomic Ru sites. Adv Mater 2020;32:e1906972.
[50] Li S, Shi M, Yu J, Li S, Lei S, Lin L, et al. Two-dimensional blue-phase CX (X = S, Se) monolayers with high carrier mobility and tunable photocatalytic water splitting capability. Chin Chem Lett 2021;32:1977–82.
[51] Zhao L, Li Y, Zhou G, Lei S, Tan J, Lin L, et al. First-principles calculations of stability of graphene-like BC3 monolayer and its high-performance potassium storage. Chin Chem Lett 2021;32:900–5.
[52] Chen W, Zhang Y, Chen G, Huang R, Wu Y, Zhou Y, et al. Hierarchical porous bimetal-sulfide bi-functional nanocatalysts for hydrogen production by overall water electrolysis. J Colloid Interface Sci 2020;560:426–35.
[53] Ren Z, Ren X, Zhang L, Fu C, Li X, Zhang Y, et al. Tungsten-doped CoP nanoneedle arrays grown on carbon cloth as efficient bifunctional electrocatalysts for overall water splitting. Chemelectrochem 2019;6:5229–36.
[54] Pan Y, Sun K, Liu S, Cao X, Wu K, Cheong WC, et al. Core-shell ZIF-8@ZIF-67-derived CoP nanoparticle-embedded N-doped carbon nanotube hollow polyhedron for efficient overall water splitting. J Am Chem Soc 2018;140:2610–8.
[55] Liu T, Liu D, Qu F, Wang D, Zhang L, Ge R, et al. Enhanced electrocatalysis for energy-efficient hydrogen production over CoP catalyst with nonelectroactive Zn as a promoter. Adv Energy Mater 2017;7:1700020.
[56] Tang C, Gan L, Zhang R, Lu W, Jiang X, Asiri AM, et al. Ternary FexCo1-xP nanowire array as a robust hydrogen evolution reaction electrocatalyst with Pt-like activity: experimental and theoretical insight. Nano Lett 2016;16:6617–21.